PHYSICAL REVIEW B **91**, 155105 (2015)

Chromium point defects in hexagonal $BaTiO_3$: A comparative study of first-principles calculations and experiments

Sanjeev K. Nayak,[1,*] Hans T. Langhammer,[2,†] Waheed A. Adeagbo,[1] Wolfram Hergert,[1]
Thomas Müller,[2] and Rolf Böttcher[3]
[1]*Institute of Physics, Martin Luther University Halle-Wittenberg, Von Seckendorff Platz 1, 06120 Halle, Germany*
[2]*Institute of Chemistry, Martin Luther University Halle-Wittenberg, Kurt Mothes Straße 2, 06120 Halle, Germany*
[3]*Faculty of Physics and Earth Sciences, University of Leipzig, Linnéstraße 5, 04103 Leipzig, Germany*
(Received 6 February 2015; revised manuscript received 17 March 2015; published 6 April 2015)

Chromium-doped hexagonal barium titanate is studied with first-principles density functional theory. The results are compared with experimental data available from electron paramagnetic resonance, x-ray diffraction, and optical absorption spectra. The probable site for the impurity atom occupancy in the lattice, their probable charge states, and the role of oxygen vacancies in their stabilization are investigated. Defect formation energy is used to analyze the role of electronic- and ionic-compensation mechanisms in stabilizing the point defect. Various atomic positions for the oxygen vacancy surrounding the impurity atom are taken into consideration in order to compare with some of the conclusions derived from experiments. Our results on the substitutional site preference and the location of oxygen vacancy in the next-neighbor surrounding of the impurity Cr are in good agreement with experiments.

DOI: 10.1103/PhysRevB.91.155105 PACS number(s): 71.20.Nr, 71.15.Mb, 61.72.J−, 71.55.−i

I. INTRODUCTION

Barium titanate ($BaTiO_3$) is a material system of fundamental importance for a wide range of technical applications and, because of the variety of phase transitions, a model system for the physical description of ferroelectricity. Besides the well-known temperature-driven phase transitions (cubic $\xrightarrow{125^\circ C}$ tetragonal $\xrightarrow{0^\circ C}$ orthorhombic $\xrightarrow{-90^\circ C}$ rhombohedral) of the cubic 3C modification (c-$BaTiO_3$) this perovskite exhibits a high-temperature phase transition into the 6H hexagonal polymorph (h-$BaTiO_3$) occurring at $\approx 1430\,^\circ C$ in air [1,2]. This modification can be stabilized down to lower temperatures either by cooling in strongly reducing atmosphere [3,4] or by doping with particular acceptor ions, which was first reported by Dickinson and Ward [5]. The 6H stacking modification forms its own temperature-driven phase transition series (hexagonal $\xrightarrow{-50^\circ C}$ orthorhombic $\xrightarrow{-199^\circ C}$ monoclinic) [6]. The influence of 3*d* transition metals (TMs) on the stabilization of h-$BaTiO_3$ has been widely investigated experimentally; see for example [3,7–11]. It has been shown that for the cases of Cr, Mn, Fe, Ni, and Cu, relatively small dopant concentrations of <1 mol % are sufficient to produce some portion of the hexagonal phase and that an impurity concentration of 2 mol % is sufficient to have nearly 100% hexagonal phase [8,12–16]. These threshold values sensitively depend both on the Ba/Ti stoichiometry and on the Sr content of the Ba source material often resulting in varying data reported by different authors. Rather small amounts of Sr significantly shift the cubic-hexagonal transition temperature to higher temperatures [17] so that sometimes in spite of a TM impurity concentration of 1–2 mol % no h-$BaTiO_3$ is detected [18,19]. The explanation of the high-temperature 3C → 6H phase transformation and the stabilization of the 6H phase down to lower temperatures is still an open question although several hypotheses have been put forward [8,11,20]. Hexagonal $BaTiO_3$ is a promising capacitor material for microwave frequency devices used for wireless communications [21–23]. Besides the application-related investigations of macroscopic properties (dielectric, magnetic, optical, etc.) of the TM-doped h-$BaTiO_3$ the investigation of the microscopic defect properties [occupation site, valence state, interaction with intrinsic defects such as oxygen vacancies (V_O), etc.] are of major importance for the basic understanding of their influence on the properties of the material. Several 3*d* dopants (Cr, Mn, Fe, Co, Ni, Cu, and Zn) are able to stabilize the hexagonal phase, but only in certain cases some of the microscopic properties are known, mainly by electron paramagnetic resonance (EPR) measurements. Moreover, there is a debate in the literature on the findings of different research groups. In this regard, the determination of the valence state of Ni_{Ti} in air-sintered $BaTiO_3$ ceramics may serve as an example. While measurements of magnetic susceptibility are interpreted with predominant Ni^{2+} [18], no Ni^{2+}, but only Ni^{3+} EPR spectra are observed [15].

Hence, theoretical studies on the electronic structure of TM-doped h-$BaTiO_3$ could be very helpful in giving additional and more detailed information on microscopic defect properties. Whereas there are a number of studies for TM-doped $BaTiO_3$ adopting various theoretical methods [24–30] for the 3C modifications (cubic, tetragonal, ...) the number of calculations for the hexagonal 6H modification is very limited. In the field of simulations using classical interatomic potentials Dawson *et al.* have presented works both on rare-earth [31] and Mn, Fe, Co, and Ni [32] doped h-$BaTiO_3$ using the force field model of Freeman *et al.* [26]. To our knowledge, first-principles density functional theory (DFT) calculations on h-$BaTiO_3$ including extrinsic point defects were performed only by Colson *et al.* [33] for Ru-doped and Li *et al.* [11] for Co-doped h-$BaTiO_3$. In both papers, neither additional electronic nor atomic point defects for charge compensation were included, thus describing only the very special defect scenario of isoelectronic doping.

---

[*] Sanjeev.Nayak@physik.uni-halle.de
[†] Hans.Langhammer@physik.uni-halle.de

The aim of the paper is to report on DFT calculations on TM-doped h-$BaTiO_3$ with a series of different defect scenarios including electronic and atomic charge compensation which are potentially realized in the material. DFT calculations of chromium-doped h-$BaTiO_3$ as isolated substitutional defect with exclusively electronic charge compensation [34] will be extended by this study. As the charge-compensating atomic defect we considered oxygen vacancies which are the most frequently occurring atomic point defects in oxide materials. The defect scenarios include the site-specific substitution of Cr impurity (isolated defects), Cr impurity together with V_O (defect complexes) for various positional configurations of V_O, and varying the supercell charge in order to model the charge state of isolated defect and defect complexes. In the present study, we focus on the Cr impurity since for this case the most extensive experimental information on the microscopic defect properties is available which could be used for comparison with the calculations. This paper, thus, signifies two primary goals. First, it brings forth the ability of DFT including necessary modifications to explain the atomistic features, and second, it shows the limitation of these first-principles instruments when it comes to analyzing the excited-state properties of Cr-doped h-$BaTiO_3$. The results of the calculations for similar defect scenarios for Mn, Fe, and Ni as impurities will be reported separately.

II. CRYSTAL STRUCTURE AND POINT DEFECT CONFIGURATION

The crystal structure of h-$BaTiO_3$ belongs to the space group $P6_3/mmc$ (No. 194). The primitive cell consists of six functional units of $BaTiO_3$ with thirty atoms in total. The crystal structure can also be considered as a layered structure of BaO_3 planes stacked along the c axis, where the smaller Ti^{4+} ions occupy the octahedral gaps between the comparably larger Ba^{2+} and O^{2-} ions. The stacking period consists of 6 BaO_3 layers of the sequence ABCBAC, so it is the 6H polytype of h-$BaTiO_3$.

There are two inequivalent positions for each constituting element, namely, Ba(1) and Ba(2) (Wyckoff positions $2b$ and $4f$), Ti(1) and Ti(2) (Wyckoff positions $2a$ and $4f$), and O(1) and O(2) (Wyckoff positions $6h$ and $12k$), where the (1) and (2) types of each element occur in the ratio 1:2 in stoichiometric h-$BaTiO_3$. Figure 1 shows the crystal structure and the inequivalent atoms in the primitive cell of h-$BaTiO_3$. The O atoms surrounding the Ti sites form TiO_6 octahedra as shown in the figure. The Ti(1)O_6 groups constitute exclusively corner-sharing octahedra of O(2) atoms, while Ti(2)O_6 groups constitute the face-sharing octahedra formed by O(1) and O(2).

As an isolated defect, chromium could substitute either Ti(1) or Ti(2) in h-$BaTiO_3$ which are denoted by $Cr_{Ti(1)}$ or $Cr_{Ti(2)}$. The occupation of Cr on Ba sites is excluded as they were found to be energetically not probable [34]. The charge states of isolated Cr defects are restricted to 2+, 3+, 4+, and 5+ as discussed in literature. This leads to eight different cases to study for isolated Cr defects. EPR investigations have shown that V_O is located away from the first coordination sphere of the Cr impurity [12]. Thus, in our study of $Cr_{Ti} - V_O$ defect complexes, we have considered configurations with V_O in the second coordination sphere to the Cr impurity together with the nearest-neighbor configurations for comparison. Related to the Ti(1) site there is one position in the first and there are two inequivalent oxygen positions in the second coordination sphere. With regard to the Ti(2) site the numbers of inequivalent oxygen sites are two for the first and four for the second coordination spheres resulting in nine inequivalent V_O due to the more complicated crystal structure of hexagonal $BaTiO_3$. Figure 1 shows the V_O locations for the defect complexes considered, called U1–U3 for $Cr_{Ti(1)} - V_O$ and V1–V6 for $Cr_{Ti(2)} - V_O$. The defect complexes U1, V1, and V2 have the vacancy in the first coordination sphere of Cr, whereas the complexes U2, U3, and V3–V6 have the vacancy in the second oxygen coordination sphere. In the case of defect complexes Cr_{Ti}^{2+} and Cr_{Ti}^{3+} are included. Thus, in this work eighteen different defect charge configurations for $Cr_{Ti} - V_O$ are considered which together with the eight charge configurations for the isolated defects lead to 26 defect scenarios to be analyzed in our study.

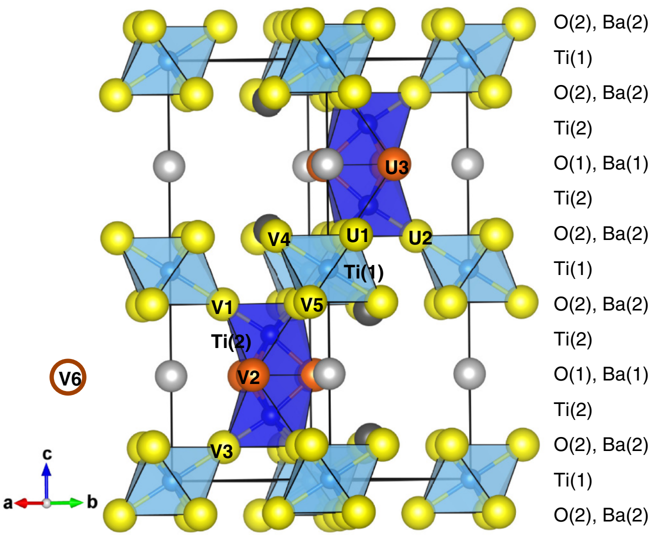

FIG. 1. (Color online) Crystal structure of h-$BaTiO_3$ showing exclusively corner-sharing oxygen octahedra of Ti(1) (light blue) and the face-sharing oxygen octahedra of Ti(2) (deep blue) sites in a primitive cell. The two inequivalent O [O(1) (orange) and O(2) (yellow)] and Ba sites [Ba(1) (light gray) and Ba(2) (gray)] are also shown. Specially marked oxygen positions related to the Ti(1) site (U1–U3) and to the Ti(2) site (V1–V6) are used to study the oxygen vacancy (see text). While the oxygen positions U1–U3 and V1–V5 lie within the primitive cell, the position V6 (shown as a brown ring) is outside the primitive cell and can be involved in the supercell.

III. COMPUTATIONAL MODELING AND ANALYSIS

A. First-principles calculation

The studies are performed with first-principles calculations based on the DFT. The plane-wave pseudopotential code Vienna *ab initio* simulation package (VASP) [35,36] is used in our studies together with the projector augmented-wave method [37], which is implemented therein. The PW'91 parametrization [38] of the generalized gradient approximation (GGA) is used as the exchange-correlation functional. The kinetic energy cutoff for the plane waves is set to

TABLE I. Comparison of the lattice parameters, Ti(1)–O(2), Ti(2)–O(1), and Ti(2)–O(2) bond lengths, and θ_A and θ_B (refer to Fig. 2) between the literature and our own calculations.

Source	a (Å)	c (Å)	d_A (Å)	d_B (Å)	θ_A (deg)	θ_B (deg)
Ref. [39] (Expt.)	5.724	13.965	1.983 [Ti(1)–O(2)]	1.983 [Ti(1)–O(2)]	55.61	124.38
			1.958 [Ti(2)–O(2)]	1.992 [Ti(2)–O(1)]	58.40	132.48
Ref. [33] (LDA USPP)	5.835	14.180				
Ref. [33] (GGA USPP)	5.684	13.846				
Present calc. (GGA PAW)	5.805	14.077	2.012 [Ti(1)–O(2)]	2.012 [Ti(1)–O(2)]	55.71	124.29
			1.978 [Ti(2)–O(2)]	2.015 [Ti(2)–O(1)]	58.65	132.31

400 eV. The supercell consists of $3 \times 3 \times 1$ repetition of the hexagonal primitive cell (total 270 atoms/supercell) and one Cr atom is substituted at a Ti site. The model generates a sample of BaCr$_x$Ti$_{1-x}$O$_3$ stoichiometry with $x = 0.0185$, which corresponds to the experimentally used impurity concentration range of $\sim$2 mol %. The supercell is relaxed by the conjugate gradient method to minimize the interatomic forces. The structural relaxation is performed within the Γ-point approximation until the interatomic forces converged below the threshold value of 25 meV/Å. Tests of relaxation with larger number of k points showed no significant variation of the structural properties. The total energy and the density of states are computed at Γ-centered $3 \times 3 \times 3$ Monkhorst-Pack k-points mesh.

Spin-polarized calculations are performed owing to the fact that Cr is a 3d transition metal. The magnetic energy is very small for such a low concentration of Cr. As a result, the self-consistent field solution could easily get stuck in a local minimum resulting in an unexpected magnetic moment. The calculations are thus thoroughly checked by applying magnetization constraints through the fixed-spin moment calculations where the total magnetic moment of the supercell is kept fixed. The magnetic moment which gives the lowest energy is taken as the true magnetic moment of the system.

B. Minimum energy lattice parameters of h-BaTiO$_3$

The lattice parameters and the Ti–O bond lengths obtained from different sources are shown in Table I. The most recent experimental lattice parameters are $a = 5.724$ Å and $c = 13.965$ Å [39]. Theoretical values obtained from the ultrasoft pseudopotentials (USPPs) with both local density approximation and GGA [33] slightly overestimated the value of a. The present calculation using the PAW pseudopotentials and the GGA gives more reasonable values of a and c which match the experimental values with a deviation of less than 1.3% and 0.8% for a and c, respectively.

The Ti(2)O$_6$ octahedra are distorted because of the slight asymmetric compression caused by the presence of the Ti(2)–Ti(2) bond along the c axis, which is locally trigonal, and the coordination with different types of O atoms. Our theoretical minimum energy crystal parameters gave $d_A < d_B$ (see Fig. 2) for the Ti(2)O$_6$ octahedron with the values 1.978 Å and 2.015 Å, respectively, and the Ti(1)–O(2) bond length of the Ti(1)O$_6$ octahedra lying in between the above values. The angles θ_A and θ_B (cf. Fig. 2 and Table I) are in good agreement with the experimental results of Akimoto *et al.* [39]. The angle made by the vertex O atoms on the opposite sides with the enclosed Ti(2) site is found to be 169.12° and 169.03° from the data of Akimoto *et al.* [39] and the present calculation, respectively, and the corresponding angles are 180° for the Ti(1) site for both cases.

C. Formation energy of defects

The charge states of a defect in a semiconductor are modeled by a charged supercell in first-principles theory and computing their defect formation energies. In the light of the known defect properties derived from experimental investigations, it is convenient to adopt the description of the Cr defects by its oxidation state. In order to bridge the different definitions, incorporating the oxidation states and charge states, in our study of defects the following conventions are adopted. An isolated substitutional Cr defect at the Ti site is represented as Cr$^{n}_{\mathrm{Ti},q}$, where q is the supercell charge and n is the oxidation state as identified in the primitive ionic model. In a similar way, the defect complexes with V$_\mathrm{O}$ are represented by Ui^n_q $(i = 1-3)$ or Vi^n_q $(i = 1-6)$ (for the definition of Ui and Vi refer to Sec. II). Thus, for example, an isolated Cr defect such as Cr$_{\mathrm{Ti(2)}}$ with supercell charges $q = 0$ and $q = +1$ corresponds to Cr$^{4+}_{\mathrm{Ti(2)}}$ and Cr$^{5+}_{\mathrm{Ti(2)}}$, respectively. Similarly, for the defect complex, for example, V6 with supercell charge $q = +1$ corresponds to Cr$^{3+}_{\mathrm{Ti(2)}} - V_\mathrm{O}$. The supercell charges may not correspond to the oxidation state of impurity atoms in a systematic manner, especially when the impurity is a multivalent TM atom.

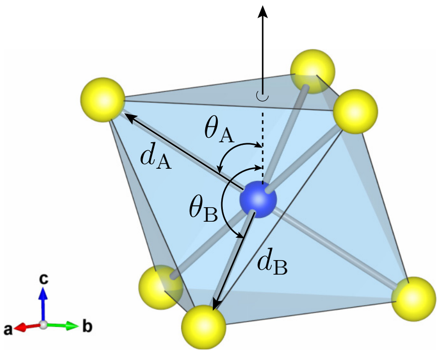

FIG. 2. (Color online) Schematic representation of an oxygen (yellow balls) octahedron and the central Ti ion (blue) with marked geometric parameters as discussed in Table I.

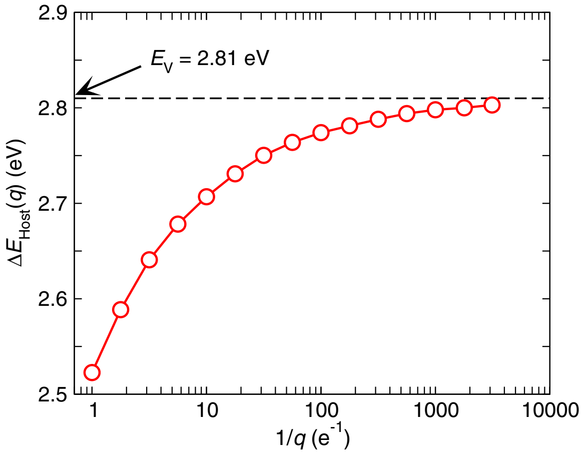

FIG. 3. (Color online) Total energy difference between the positively charged (q) and the neutral unit cell of h-BaTiO$_3$[$\Delta E_{Host}(q)$] as a function of ($1/q$). The asymptote of $\Delta E_{Host}(q)$ gives the value of E_V which is estimated to be 2.81 eV from GGA calculations.

The formation energy of a point defect (D) in charge state q, $E_{form}(D,q)$, is given by [40–42]

$$E_{form}(D,q) = E(D,q) - E_{Host} + \sum_i p_i n_i \mu_i + q(E_V + \Delta E_F). \quad (1)$$

Here, $E(D,q)$ and E_{Host} are the total energies of the supercell with defect and the host supercell of similar size, respectively. The equation is balanced by using the chemical potentials (μ_i) of the elemental species (i), their numbers n_i and the factor p_i, where $p_i = -1$ for atoms added to the host supercell and $p_i = +1$ for atoms removed from the host supercell in order to construct the defect supercell. E_V is the valence band maximum of the host and ΔE_F represents the position of the Fermi level in the band gap referenced from E_V. The total energies of relaxed supercells obtained from DFT with GGA are taken for the computation of E_{form}.

The valence band maximum, E_V, is defined as $\lim_{q\to 0} \Delta E_{Host}(q)$, where $\Delta E_{Host}(q)$ is given by [43]

$$\Delta E_{Host}(q) = \left[\frac{E_{Host}(q=0) - E_{Host}(q)}{q}\right]. \quad (2)$$

$E_{Host}(q)$ is the total energy of the unit cell of h-BaTiO$_3$ for various hole concentrations. The value of E_V for h-BaTiO$_3$ estimated from the asymptote of $E_{Host}(q)$ as a function of $1/q$, as shown in Fig. 3, is found to be 2.81 eV. The Kohn-Sham eigenvalue for the highest occupied level at the Γ point is found to be 2.76 eV, which is lower than E_V obtained from Eq. (2) by only 0.05 eV. Thus, both approaches of estimation of E_V are reliable; however, we have used the former approach with the value of $E_V = 2.81$ eV in our analysis. The Fermi level is measured relative to E_V, i.e., expressed by $E_V + \Delta E_F$ for $0 \leqslant \Delta E_F \leqslant E_g$, with E_g being the experimental optical band gap of the host semiconductor.

The transition level between the two charge states q and $q'[\varepsilon(q/q')]$ is defined as the energy at which the formation energies of the two charge states are equal. The transition level is thus given as

$$\varepsilon(q/q') = \frac{E_{form}(D,q) - E_{form}(D,q')}{q' - q}. \quad (3)$$

The position of $\varepsilon(q/q')$ in the band gap defines the nature of defect states (shallow or deep defects) and could be accessed by optical spectroscopy and transport measurements [44].

1. Chemical potentials for formation energy

The discussion of formation energies is an instrument to map the ground-state DFT calculations to the thermodynamic conditions accessible in experiment. The absolute values of formation energies are limited by the choice of the chemical potentials since the suitable chemical potentials that correspond to the experimental growth conditions are unknown. As a result, the formation energies are calculated at selected chemical potentials which represent the extreme boundaries for a chemical reaction. It is useful to linearly interpolate the formation energies within the extreme values of the chemical potentials. Thus, the relative comparison of the formation energies helps in judging the relative stability of various defects at a given environmental condition. To a reasonable assumption, except for the gaseous components which can be dealt with thermodynamically, the chemical potential of other components can be derived from the total energies of the bulk or molecular species [44]. The following chemical potentials have been used in our studies:

$$\begin{aligned} \mu_{Ti} &= E(TiO_2) - 2\mu_O, \\ \mu_{Cr} &= \tfrac{1}{2}\left[E(Cr_2O_3) - 3\mu_O\right], \end{aligned} \quad (4)$$

where μ_O is treated as a variable with an estimated upper limit of

$$\mu_O^{max} = \tfrac{1}{2} E(O_2), \quad (5)$$

often called an "oxygen-rich" condition, where $E(O_2)$ is the total energy of a free, isolated O_2 molecule in the triplet state at $T = 0$ K [45].

The chemical potentials are calculated from DFT using the GGA functional. The total energy $E(TiO_2)$ is derived from rutile structure with lattice parameters $a = 4.66$ Å and $c = 2.96$ Å. The total energy $E(Cr_2O_3)$ is derived from the trigonal crystal structure (Cr spins arranged antiferromagnetically) with lattice parameter $a = b = c = 5.41$ Å and $\alpha = \beta = \gamma = 55.11^\circ$. The values of the chemical potentials are $\mu_O^{max} = -4.93$ eV, $\mu_{Ti} = -17.12$ eV, and $\mu_{Cr} = -14.33$ eV computed from Eq. (4) and Eq. (5).

In order to relate the oxygen chemical potential to experimentally given values for temperature and oxygen partial pressure (p_{O_2}) the thermodynamic expression

$$\mu_O(T,p_{O_2}) = \mu_O(T,p^\circ) + \frac{1}{2}kT \ln\left(\frac{p_{O_2}}{p^\circ}\right) \quad (6)$$

is used, where, p° is the standard pressure of 1 bar. The values of $\mu_O(T,p^\circ)$ are taken from thermochemical tables [46]. To link the values of μ_O of Eq. (4) to the thermodynamic expression of Eq. (6) we choose a common reference as $\mu_O(0K,p) = \mu_O^{max}$, following the idea of Reuter *et al.* [45], and present the chemical potential of oxygen as $\Delta\mu_O$. Figure 4 shows the relation between $\Delta\mu_O$ and p_{O_2} calculated according

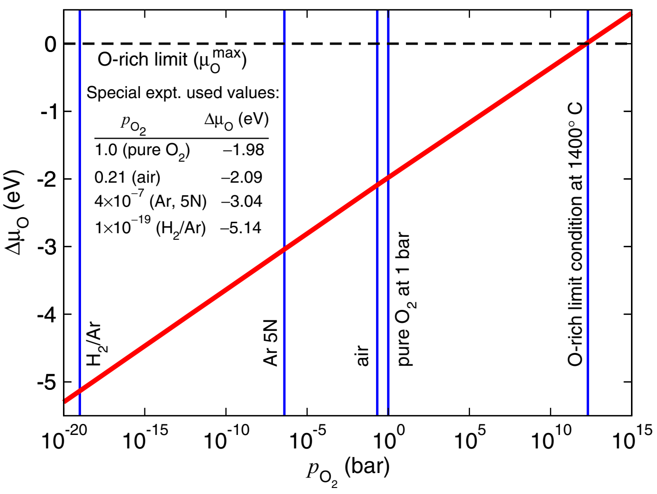

FIG. 4. (Color online) Relation between oxygen partial pressure (p_{O_2}) and the relative chemical potential of oxygen ($\Delta\mu_O$) at T = 1400 °C. The estimation is done by using Eq. (6) together with the absolute value for μ_O in the O-rich condition [Eq. (5)] set to zero.

to Eq. (6) at 1400 °C, which is the sintering temperature of the ceramic $BaTiO_3$ samples. At this temperature, the thermodynamic equilibrium between the atomic defects in the sample and the environment with respect to oxygen partial pressure can be assumed. The experimentally covered range of p_{O_2} from strongly reducing conditions using a gas mixture of H_2/Ar to pure oxygen at 1 bar corresponds to $\Delta\mu_O$ ranging from −5.14 eV to −1.98 eV, respectively. The values are marked in Fig. 4.

2. GGA total energies and beyond

DFT with the GGA provides an elegant method for calculation of the total energies of chemical systems. The formation energies derived from the DFT total energies also possess a high degree of reliability. It is well known that GGA has a limitation in treating the correlation effects and, hence, the localization effects of the valence band density of states are underrated [47]. This leads to a material-specific underestimation of the band gap of semiconductors. The band gap of h-$BaTiO_3$ is found to be 1.73 eV in GGA while the optical band gap is about 3.4 eV, which is an underestimation of 50% of the predicted value.

There are correction schemes, such as adding Coulomb correlation U to the GGA functional (GGA+U) and the self-interaction correction method, which improve the electronic density of states. The corrections are usually applied to selected orbitals of specific elements in the solid and, hence, the total energy derived from such schemes is biased and might influence the E_{form}. In addition, the value of U is not transferable to elementary systems from which chemical potentials are derived [48]. Hence, this poses a problem for the studies of defect properties. Apart from the orbital-specific treatments, the Heyd-Scuseria-Ernzerhof hybrid-functional method [49] has been successfully applied to the study of point defects [50]. However, such calculations are very demanding, especially for such a large supercell as used in our studies.

This situation drives us to adopt empirical postprocessing (PP) corrections as suggested by Lany and Zunger [48]. The postprocessing is applied to overcome two types of limitations, namely, opening the band gap from the DFT value to that of the experimental value and accounting for the finite size of supercells which causes a too large concentration of defects. Details of the PP corrections used in our analysis are discussed in the Appendix. The postprocessed formation energy, $E_{\text{form}}^{\text{PP}}(\text{D},q)$, is given by Eq. (A1). We have a fairly large supercell where the concentration of defects has been matched with the experimental range. Hence, the finite-size corrections play only a minor role. The relative shift of the band edge ΔE_V is the main contribution to the PP correction for charged defects through the term $q\Delta E_V$.

The PP corrections in the form mentioned above influence the shallow defect states which have stronger hybridization to the extended states of either VB or CB. However, the nature of corrections applicable to deep defects is an open question. A linear extrapolation of the position of the transition level of deep defects in the band gap by comparing the GGA and GGA+U total energies has been reported [51–53]. The deep defects are due to the localized states which are least influenced by the shift of band edges of VB or CB. Hence, we ignore deep defect corrections.

IV. RESULTS AND DISCUSSION

For the isolated Cr defects substituted at Ti(1) and Ti(2) sites total energy calculations are performed for supercell charges $q = -2, -1, 0$, and 1. Some of the physical properties obtained from different charge calculations for the isolated defects are shown in Table II. In a similar manner, various configurations (Ui and Vi) of defect complex $\text{Cr}_{\text{Ti}} - \text{V}_{\text{O}}$ are studied for supercell charges $q = 0$ and $q = +1$. The physical properties obtained for defect complexes are summarized in Table III where the distance of the oxygen vacancy from Cr impurity ($d_{\text{Cr}-\text{V}_\text{O}}$) is derived from the unrelaxed supercell.

It must be remarked that the relationship between the supercell charges and the charge state (also known as the oxidation state) of the impurity may not correspond one-to-one. In the case of TM impurities, the charge state of the impurity atom could be determined from the local magnetic moment analysis (m_{Cr}). For example, an isolated Cr defect in $BaTiO_3$ for supercell charge $q = 0$ is expected to be in the Cr^{4+} state (d^2 configuration). According to Hund's rule, we expect $2\mu_B$ for the magnetic moment of Cr. Indeed, our calculations show that the magnetic moments of $\text{Cr}_{\text{Ti(1)}}$ and $\text{Cr}_{\text{Ti(2)}}$ defects for $q = 0$ are about $1.8\mu_B$ (Table II), clearly suggesting that the valence state of Cr for this case is Cr^{4+}. The general form of the defect can thus be written as $\text{Cr}_{\text{Ti(1)}}^{4+}$ and $\text{Cr}_{\text{Ti(2)}}^{4+}$. Similarly, for the supercell charges $q = +1$ and $q = -1$ for isolated defects we find that m_{Cr} are about $2.5\mu_B$ and $0.95\mu_B$, respectively, for both Ti site occupancies, suggesting that the electrons are removed from or added to the Cr impurity. This allows us to assign the oxidation states as $\text{Cr}_{\text{Ti}}^{3+}$ and $\text{Cr}_{\text{Ti}}^{5+}$ for supercell charges $q = +1$ and $q = -1$ without any ambiguity. Unlike the previous cases, however, for the supercell charge $q = -2$ the magnetic moment does not change from that of the supercell charge $q = -1$. This suggests that the extra electron added to the system is delocalized and found in the conduction

TABLE II. Comparison of the calculated physical properties for isolated $\mathrm{Cr}^{n+}_{\mathrm{Ti},q}$ defect, where q is the supercell charge and n is the valence state. M is the total magnetic moment of the supercell and m_{Cr} is the magnetic moment of Cr. The distortion of the Cr surrounding O octahedron is characterized by d_A, d_B, θ_A, and θ_B (see Fig. 2). E_{form} and $E^{\mathrm{PP}}_{\mathrm{form}}$ are the formation energies obtained from Eq. (1) and Eq. (A1), respectively, using $\Delta\mu_{\mathrm{O}}$ (air) (refer to Sec. III C). ΔE_{form} and $\Delta E^{\mathrm{PP}}_{\mathrm{form}}$ are the formation energy differences as referenced from the lowest value of formation energy obtained between the two sites.

Property	Site	[a]$\mathrm{Cr}^{3^*+}_{\mathrm{Site},-2}$	$\mathrm{Cr}^{3+}_{\mathrm{Site},-1}$	$\mathrm{Cr}^{4+}_{\mathrm{Site},0}$	$\mathrm{Cr}^{5+}_{\mathrm{Site},+1}$
M (μ_B)	Ti(1)	2.85	3.00	2.00	1.00
	Ti(2)	2.86	3.00	2.00	1.00
m_{Cr} (μ_B)	Ti(1)	2.57	2.58	1.84	0.97
	Ti(2)	2.52	2.53	1.80	0.93
d_A (Å)	Ti(1)	2.022	2.021	1.975	1.926
	Ti(2)	1.970	1.965	1.870	2.056
d_B (Å)	Ti(1)	2.022	2.021	1.975	1.926
	Ti(2)	2.048	2.055	2.062	1.784
θ_A (deg)	Ti(1)	56.16	56.22	56.11	55.98
	Ti(2)	49.48	49.51	52.41	49.03
θ_B (deg)	Ti(1)	123.84	123.78	123.89	124.02
	Ti(2)	123.02	123.16	124.69	118.45
E_{form} (eV)	Ti(1)	2.924	1.246	0.556	0.163
	Ti(2)	2.826	0.909	0.090	−0.818
ΔE_{form} (eV)	Ti(1)	0.098	0.337	0.466	0.981
	Ti(2)	0.000	0.000	0.000	0.000
$E^{\mathrm{PP}}_{\mathrm{form}}$ (eV)	Ti(1)	3.833	0.738	0.556	0.738
	Ti(2)	3.727	0.274	0.090	−0.149
$\Delta E^{\mathrm{PP}}_{\mathrm{form}}$ (eV)	Ti(1)	0.106	0.464	0.466	0.887
	Ti(2)	0.000	0.000	0.000	0.000

[a]The magnetic moment analysis gives an oxidation state of 3+, while charge balance considerations suggest a charge state of 2+.

band. This picture corroborates with the location of the Fermi level in the conduction band when analyzed from the density of states [34]. In order to take proper consideration of these factors, the isolated Cr defect for the supercell charge $q = -2$ is written as $\mathrm{Cr}^{3^*+}_{\mathrm{Ti}}$ meaning that the oxidation state of Cr is 3+, even though the charge balance demands it to be in charge state 2+. A similar situation also occurs for the defect complex in supercell charge $q = 0$, where it is written as $\mathrm{Cr}^{3^*+}_{\mathrm{Ti}} - \mathrm{V}_{\mathrm{O}}$ (refer to Table III).

The formation energies E_{form} and $E^{\mathrm{PP}}_{\mathrm{form}}$ derived as a function of chemical potential of oxygen $\Delta\mu_{\mathrm{O}}$ for the isolated defects and defect complexes with V_{O} are shown in Figs. 5(a) and 5(b), respectively. For a comparison with experimentally relevant growth or annealing conditions the corresponding values of the oxygen partial pressure, p_{O_2}, are shown in the upper scale of the abscissa. Since the formation energies of the isolated $\mathrm{Cr}_{\mathrm{Ti(2)}}$ defects are systematically lower than that of $\mathrm{Cr}_{\mathrm{Ti(1)}}$ defects, the data of only the former are plotted in Fig. 5 for clarity. For the same reason, only the defect formation energies for the supercell charge $q = +1$ are shown for $\mathrm{Cr}_{\mathrm{Ti}} - \mathrm{V}_{\mathrm{O}}$ defect complexes in Fig. 5.

We discuss the DFT results in relation to the defect properties obtained from the experimental studies of Refs. [12,13]. The dependencies of E_{form} and $E^{\mathrm{PP}}_{\mathrm{form}}$ on $\Delta\mu_{\mathrm{O}}$ [see Figs. 5(a) and 5(b)] show that $\mathrm{V6}^{3+}_{+1}$ is the lowest lying and, thus, the most probable defect in Cr-doped $\mathrm{BaTiO_3}$ for a wide range of growth conditions with $\Delta\mu_{\mathrm{O}} \leqslant -2.0$ eV which corresponds to oxygen partial pressures $\leqslant 1$ bar (approximately). At higher $\Delta\mu_{\mathrm{O}}$ the most probable defect is the $\mathrm{Cr}^{5+}_{\mathrm{Ti(2)},+1}$ which is found both in GGA and GGA+PP calculations. Based on the combined investigations of electron paramagnetic resonance (EPR), x-ray diffraction (XRD), and wavelength-dispersive electron probe microanalysis (WDX-EPMA) on samples grown with a nominal dopant concentration of 2.0 mol % and a sintering temperature of 1400 °C in air, it is found that 50%–60% of the dopant incorporated into the grown grains is in the +3 oxidation state, whereas the remnant is assumed to be in the tetravalent charge state, which is EPR silent [12].

After annealing these samples in pure oxygen ($p_{\mathrm{O}_2} = 1$ bar) at 1200 °C, the majority of Cr^{3+} is oxidized, and thus only a small amount of Cr^{3+} is detected [13]. While for $p_{\mathrm{O}_2} \leqslant 1$ bar the experiments and calculations coincide very

TABLE III. Comparison of the calculated physical properties for the $\mathrm{Cr}_{\mathrm{Ti}} - \mathrm{V}_{\mathrm{O}}$ complexes for various lattice positions of V_{O}. The first four columns show the nomenclature described in Sec. II, the corresponding crystallographic sites for V_{O} and $\mathrm{Cr}_{\mathrm{Ti}}$, and the distance between Cr and V_{O} ($d_{\mathrm{Cr}-\mathrm{V_O}}$) obtained from perfect host lattice. M is the total magnetic moment of the supercell and m_{Cr} is the magnetic moment of the Cr atom. E_{form} and $E^{\mathrm{PP}}_{\mathrm{form}}$ are the formation energies obtained from Eq. (1) and Eq. (A1) using $\Delta\mu_{\mathrm{O}}$ (air). ΔE_{form} and $\Delta E^{\mathrm{PP}}_{\mathrm{form}}$ are the formation energy differences as referenced from the lowest value of formation energy which is set to zero. The units of the physical quantities are the same as in Table II.

				$q = 0$, [a]$(\mathrm{Cr}^{3^*+}_{\mathrm{Ti}} - \mathrm{V}_{\mathrm{O}})$						$q = +1$, $(\mathrm{Cr}^{3+}_{\mathrm{Ti}} - \mathrm{V}_{\mathrm{O}})$					
Case	V_{O}	Cr	$d_{\mathrm{Cr}-\mathrm{V_O}}$	M	m_{Cr}	E_{form}	ΔE_{form}	$E^{\mathrm{PP}}_{\mathrm{form}}$	$\Delta E^{\mathrm{PP}}_{\mathrm{form}}$	M	m_{Cr}	E_{form}	ΔE_{form}	$E^{\mathrm{PP}}_{\mathrm{form}}$	$\Delta E^{\mathrm{PP}}_{\mathrm{form}}$
U1	O(2)	Ti(1)	2.01	4.00	3.07	1.287	0.519	1.287	0.489	3.0	2.52	−0.225	0.963	0.408	0.084
U2	O(1)	Ti(1)	4.57	2.85	2.59	0.785	0.017	2.883	2.085	3.0	2.60	−1.159	0.029	−0.116	0.376
U3	O(2)	Ti(1)	4.59	2.82	2.59	1.531	0.763	3.448	2.650	3.0	2.60	−0.391	0.797	0.236	0.728
V1	O(2)	Ti(2)	1.98	4.00	2.95	1.314	0.546	1.743	2.517	3.0	2.47	−0.418	0.770	0.289	0.781
V2	O(1)	Ti(2)	2.01	4.00	2.99	0.768	0.000	0.798	0.000	3.0	2.44	−0.808	0.380	−0.111	0.381
V3	O(2)	Ti(2)	4.10	2.47	2.48	1.466	0.698	3.824	3.026	3.0	2.53	−0.457	0.731	0.242	0.734
V4	O(2)	Ti(2)	4.39	2.73	2.54	1.493	0.725	3.498	2.700	3.0	2.55	−0.435	0.066	0.256	0.748
V5	O(2)	Ti(2)	4.54	2.73	2.54	1.514	0.746	3.475	2.677	3.0	2.55	−0.416	0.074	0.273	0.765
V6	O(1)	Ti(2)	4.77	2.70	2.52	0.769	0.001	2.985	2.187	3.0	2.53	−1.188	0.000	−0.492	0.000

[a]The magnetic moment analysis gives an oxidation state of 3+, while charge balance considerations suggest a charge state of 2+.

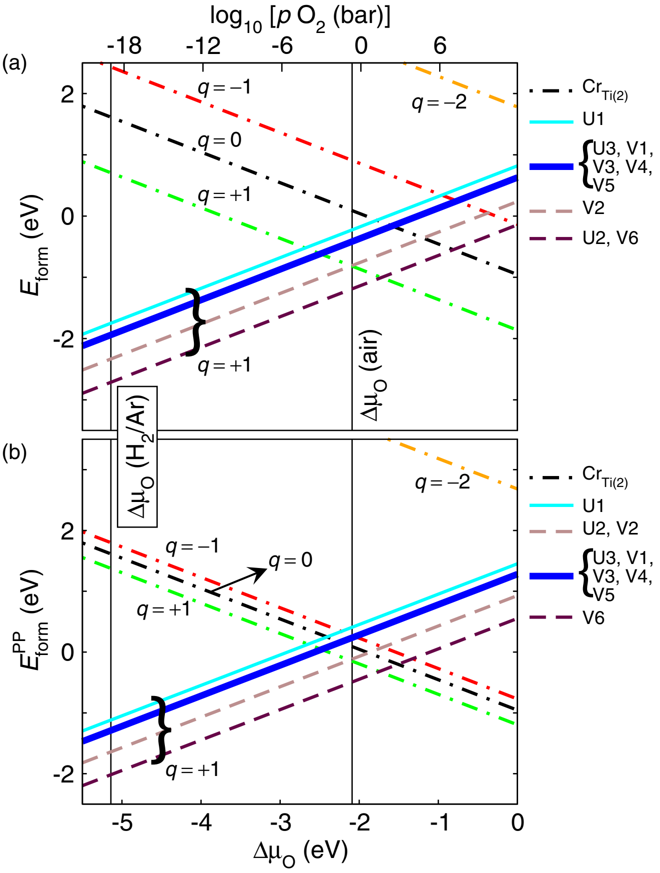

FIG. 5. (Color online) The formation energies E_{form} (a) and $E^{\mathrm{PP}}_{\mathrm{form}}$ (b) as a function of chemical potential of oxygen $\Delta\mu_{\mathrm{O}}$ for substitutional $\mathrm{Cr}_{\mathrm{Ti(2)}}$ defect and $\mathrm{Cr}_{\mathrm{Ti}} - \mathrm{V}_{\mathrm{O}}$ defect complexes. The upper abscissa scale corresponds to the value of oxygen partial pressure (p_{O_2}) from experiments, which is calculated as described in Sec. III C. Experimentally relevant oxidizing and the reducing conditions are shown as vertical lines.

well, the calculations show that $\mathrm{Cr}^{5+}_{\mathrm{Ti(2)},+1}$ is more probable than $\mathrm{V6}^{3+}_{+1}$ for increasing p_{O_2}, which seems to be contrary to the experimental result since $\mathrm{Cr}^{5+}_{\mathrm{Ti}}$ is an EPR-active center in $\mathrm{BaTiO_3}$ [54,55], which was never observed in the oxidized hexagonal samples. This discrepancy is less developed for the GGA+PP calculations where the difference in the formation energy between $\mathrm{Cr}^{5+}_{\mathrm{Ti(2)},+1}$ and $\mathrm{Cr}^{4+}_{\mathrm{Ti(2)},0}$ amounts only to about 0.34 eV suggesting that $\mathrm{Cr}^{4+}_{\mathrm{Ti(2)},0}$ is a competing defect.

After annealing the samples in a strongly reducing atmosphere, which introduces $\mathrm{V_O}$ into the samples, the amount of Cr^{3+} increased significantly and it is assumed that the remnant (roughly estimated <10%) is in the divalent state [13]. Since the formation energies of the defect complex with supercell charge $q = +1$ was found to be systematically lower than the energies of the complex with charge $q = 0$ for the whole range of oxygen chemical potential, this fact could not be verified. It must be noted, however, that the charge state of 2+ must be carefully treated as already mentioned.

From EPR investigations the location of $\mathrm{V_O}$ in the first coordination sphere of Cr is ruled out [12], thus concluding that charge-compensating $\mathrm{V_O}$ is located away from the Cr impurity atom, although the precise location of the $\mathrm{V_O}$ has not been identified. The formation energies of Fig. 5 show that the complexes U1, V1, and V2, which are the configurations where $\mathrm{V_O}$ is located in the first coordination sphere of Cr (U1 for $\mathrm{Cr}_{\mathrm{Ti(1)}}$ and V1 and V2 for $\mathrm{Cr}_{\mathrm{Ti(2)}}$) have higher formation energies. On the other hand, the configurations U2 and V6 (GGA), and V6 (GGA+PP), respectively, have the lowest formation energies. U2 and V6 are the configurations where the $\mathrm{V_O}$ is located in the next-neighboring shell of $\mathrm{Cr}_{\mathrm{Ti(1)}}$ and $\mathrm{Cr}_{\mathrm{Ti(2)}}$, respectively (see Table III). Thus, our study corroborates very well the experimental observation revealing that $\mathrm{V_O}$ is located away from the Cr impurity atom.

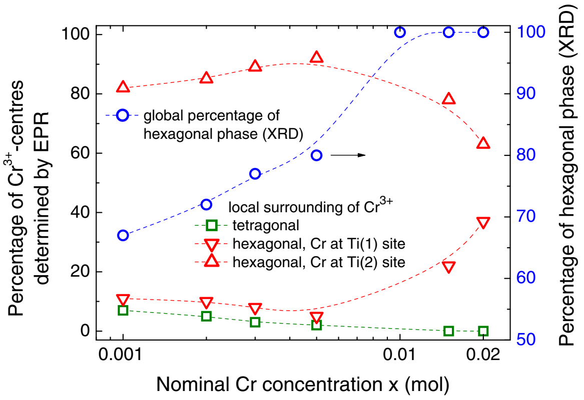

FIG. 6. (Color online) Percentage of Cr^{3+} centers at different lattice sites of as-sintered Cr-doped $\mathrm{BaTiO_3}$ derived from EPR spectroscopy together with the percentage of hexagonal phase (derived from XRD) as a function of the nominal concentration of Cr (redrawn from Ref. [13]).

Dawson *et al.* have considered only the first coordination sphere of the 3*d* TM impurity atoms and found that the charge-compensating oxygen vacancy is located in the face-sharing O(1) plane of the Ti(2) octahedra [32]. This coincides very well with our results as $\mathrm{V_O}$ of the defect complex V6 lies in that plane. But the inclusion of the second oxygen coordination sphere of Cr showed that the vacancy position in the first coordination sphere (V2) is less likely than in the second (V6).

It is worthwhile to mention that the location of Cr in the defect complex is also satisfactorily obtained by the calculations. Taking into account the two lower formation energy lines of Fig. 5 we find that they describe the defect configurations U2, V2, and V6. While relative values of formation energies change slightly between U2 and V2 from GGA to GGA+PP, the configuration V6 is found to possess the lowest formation energy consistently in GGA and GGA+PP calculations. Thus, one would expect that the relative abundance of $\mathrm{Cr}_{\mathrm{Ti(2)}}$ (configurations V2 and V6) would be slightly larger than $\mathrm{Cr}_{\mathrm{Ti(1)}}$ (configuration U2). This corresponds very well with the experimental finding that Ti(2) is the preferred incorporation site for Cr (see Fig. 6). As the percentage of Cr content in the sample is increased, the probability of Ti(1) site occupation increases and reaches about 40% of the total amount of incorporated Cr^{3+} at a nominal Cr concentration of 2 mol % (refer to Fig. 6). Our findings for the location of Cr in the defect complex are only in partial

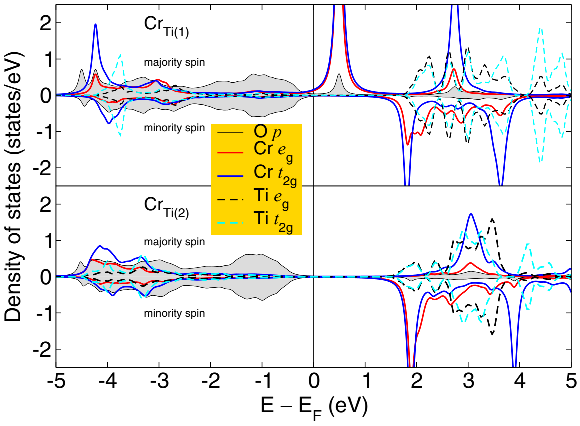

FIG. 7. (Color online) Density of states of O-p and the t_{2g} and e_g states of Cr and Ti for the isolated $\mathrm{Cr}_{\mathrm{Ti}(1)}$ and $\mathrm{Cr}_{\mathrm{Ti}(2)}$ defects.

agreement with Dawson *et al.* [32], who stated a considerable preference for Ti(2) site occupation compared to the Ti(1) site.

The formation energy difference ΔE_{form} between the Cr substitution at the Ti(1) and Ti(2) sites each for isolated defects (Table II) also suggests that the probability of Cr occurring at the Ti(2) site is higher than that at the Ti(1) site. The ΔE_{form} increases as the charge of the supercell is increased [34], a conclusion also derived from the postprocessing data of $\Delta E_{\mathrm{form}}^{\mathrm{PP}}$. The trend in the total magnetic moment M and the magnetic moment of Cr (m_{Cr}) found for the various charge states shows that the additional charge (electron for $q = -1$ and hole for $q = +1$) is captured by the Cr, except for the case of $q = -2$.

In order to demonstrate the qualitative differences of the orbital hybridization and crystal field splittings of isolated Cr defects on the Ti(1) and Ti(2) sites, the electronic density of states (DOS) for the t_{2g} and e_g states of Cr is shown and compared in Fig. 7. The DOS in the occupied states is broader in the deeper valence band for $\mathrm{Cr}_{\mathrm{Ti}(2)}$ as compared to $\mathrm{Cr}_{\mathrm{Ti}(1)}$ suggesting a stronger hybridization of Cr t_{2g} and e_g states with the p orbitals of surrounding oxygen atoms, which results in lowering of the total energy. Thus, the preferable occupancy site for Cr is on the Ti(2) site as compared to the Ti(1) site.

A general tendency is observed in the formation energies (both for GGA and GGA+PP) of defect complexes. The supercell charge $q = +1$ for the defects has lower values of formation energies than the neutral supercells $q = 0$ (refer to Table III). Taking into consideration the charge balance in point defects this establishes more firmly that the oxidation states of Cr in the defect complex is 3+ for a wide range of growth conditions. This is in agreement with the observed trend in magnetic moments and the experimental inferences.

As of now, the comparison between theory and experiment has been done for the types of defects which were detected experimentally and comparing their formation energies to ascertain their probability of occurrence. Highly reducing conditions cause a strong increase of the concentration of Schottky-type oxygen vacancies which act as donors due to their release of free electrons into the conduction band, and hence, increases the Fermi level. Thus, it is worthwhile to compare the formation energy of defects as a function of Fermi level position. Figure 8 compares E_{form} and $E_{\mathrm{form}}^{\mathrm{PP}}$ as a function of the Fermi level position (ΔE_{F}) for oxidizing [Figs. 8(a) and 8(b)] and reducing [Figs. 8(c) and 8(b)] conditions, respectively. Among the different charge states considered for a defect only the charge states with lowest formation energies are shown as a function of ΔE_{F}. We find that the defect complex $\mathrm{V2}_0^{3*+}$ (as favored by Dawson *et al.* [32]) becomes more probable than the $\mathrm{V6}_{+1}^{3+}$ when the Fermi level moves towards the CB. This transition occurs for the GGA+PP case at a lower Fermi level than for GGA [notice carefully the legend colors in Figs. 8(c) and 8(d)], both of which correspond well—at least as a trend—with the experimental observations.

The formation energies as a function of ΔE_{F} also give a hint on the charge transition levels of a defect through Eq. (3). The point of intersection of formation energy lines as a function of ΔE_{F} for two charge states is defined as the transition level between the two charges (shown in parentheses in Fig. 8) for that defect. In principle, the transition level of defects lying in the band gap region corresponds to defect levels which are optically active [44]. In the present study, the optical absorption spectroscopy is used as a tool to compare the transition levels obtained from theoretical calculations. Since the time scale of the optical phenomena is very small compared to the ionic relaxation, it is assumed that the supercell relaxation does not play an important role in the optical transitions. In the present analysis the formation energies of charged defects are calculated from relaxed supercells. The Frank-Condon shifts are thus implicitly taken into account. The transition levels estimated from theoretical studies are independent of $\Delta\mu_{\mathrm{O}}$. The change of the optical absorption spectra for samples equilibrated at different environmental conditions is reflected through the relative abundance of different defects at respective environmental conditions.

Figure 9 shows the optical absorption spectra of Cr-doped $\mathrm{BaTiO_3}$ ceramics both for samples equilibrated in air and for samples equilibrated under strongly reducing conditions [13]. The absorption bands P1 and P3 occurring under both environmental conditions are attributed to a charge transfer transition (transition from VB to the defect level in the band gap) as $\mathrm{Cr}^{3+} \rightarrow \mathrm{Cr}^{2+} + h^+$ (h^+ implies a hole in the VB). The absorption band P2 of the air-sintered sample is also attributed to a charge transfer process, but for the Cr^{4+} defect (occurring in 40%–50% in the samples) described by transformation $\mathrm{Cr}^{4+} \rightarrow \mathrm{Cr}^{3+} + h^+$. And finally, the weak absorption band P4 occurring in the strongly reduced samples is explained by intervalence transitions (transition from defect level to the CB) concerning Cr^{2+} which has a rather low concentration ($<10\,\%$; see above). This excitation is attributed to $\mathrm{Cr}^{2+} \rightarrow \mathrm{Cr}^{3+} + e^-(\mathrm{CB})$. In view of the low intensity of P4, the forbidden *d-d* transitions of Cr^{3+} or Cr^{2+} cannot be excluded [13].

The transitions of interest are $\mathrm{Cr}^{4+/3+}[\varepsilon(0/-)]$ for the isolated Cr defects (which appear only for $\mathrm{Cr}_{\mathrm{Ti}(1)}$) and $\mathrm{Cr}^{3+/2+}[\varepsilon(+/0)]$ for the $\mathrm{Cr}_{\mathrm{Ti}} - \mathrm{V}_{\mathrm{O}}$ defect complexes. These transition levels are extracted from Fig. 8 for GGA (blue lines) and GGA+PP (red lines) and plotted in the common platform of Fig. 10 together with the experimental transition levels (black lines) derived from absorption peaks P1–P4 as

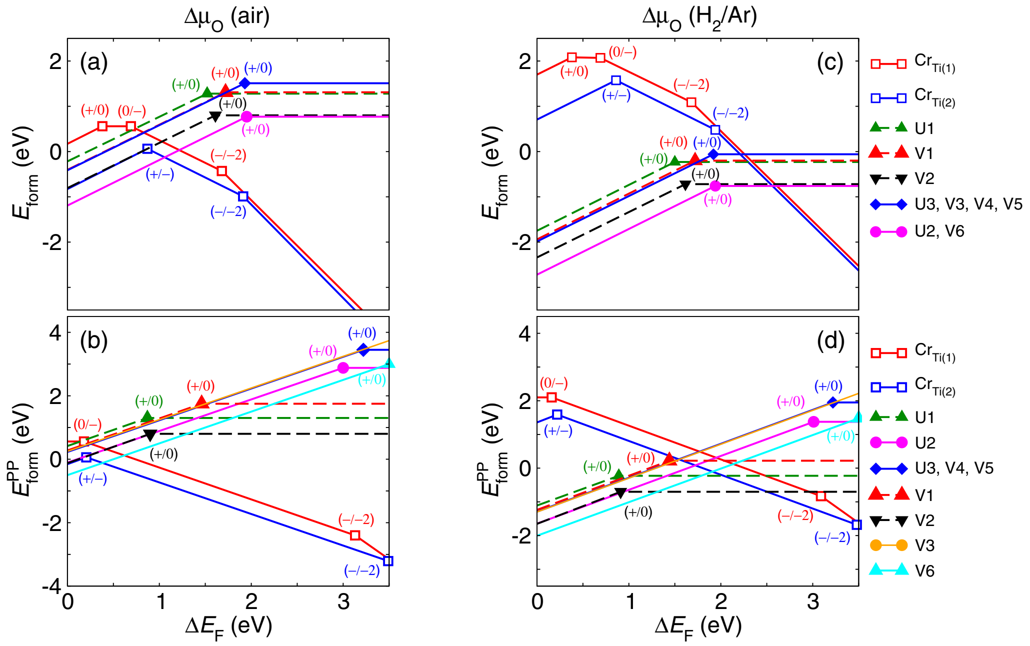

FIG. 8. (Color online) The formation energies E_{form} and $E_{\text{form}}^{\text{PP}}$ of the stable charge states of substituted Cr_{Ti} defects and $\text{Cr}_{\text{Ti}} - \text{V}_{\text{O}}$ defect complexes shown as a function of Fermi level (ΔE_{F}) at the oxidizing (air) [(a) and (b)] and the reducing (H$_2$/Ar) conditions [(c) and (d)], respectively. The intersecting points (q/q') are the charge transition levels $\varepsilon(q/q')$ of Eq. (3).

shown in Fig. 9. The band gap region for GGA+PP and that of the experimental data are similar; however, the band gap obtained from GGA is smaller. Its CB maximum is shown as a dashed line in Fig. 10.

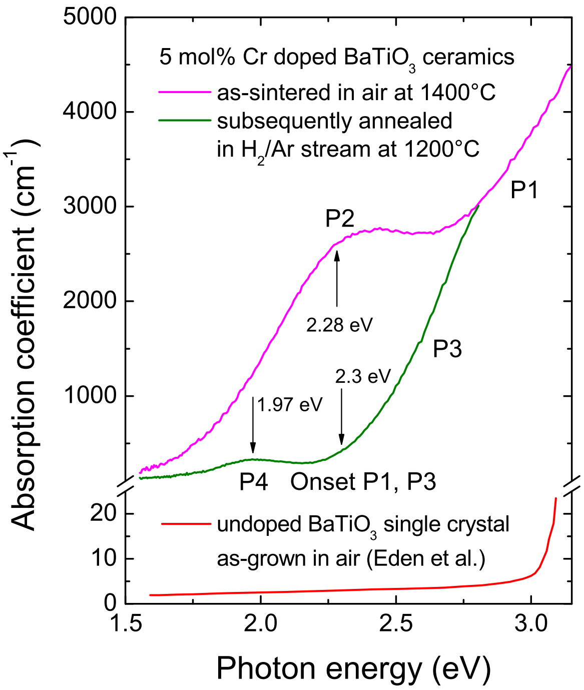

FIG. 9. (Color online) Optical absorption spectra (unpolarized light) of 5.0 mol % Cr-doped thinned BaTiO_3 ceramics sintered and annealed at two different environmental partial pressures of oxygen (redrawn from Ref. [13]). The spectrum of an undoped BaTiO_3 single crystal [56] is shown for comparison.

Comparing the charge transfer transitions of Fig. 10 a qualitative trend can be matched between calculations and experiment. Similarly to the transition levels derived from experiments, the transition level $\text{Cr}^{4+/3+}$ of isolated defects ($\text{Cr}_{\text{Ti(1)}}$) is closer to the VB maximum than the transition levels $\text{Cr}^{3+/2+}$ of defect complexes. While the transition levels of defect complexes are either in the CB or at shallow region near the CB for GGA (refer to the dashed line of Fig. 10), the transition levels from GGA+PP are spread in the band gap region for different configurations of defect complexes. The defect complex configurations where the V_{O} is located in the nearest neighborhood to the Cr defect (U1, V1, and V2) have transition levels deep in the band gap. On the other

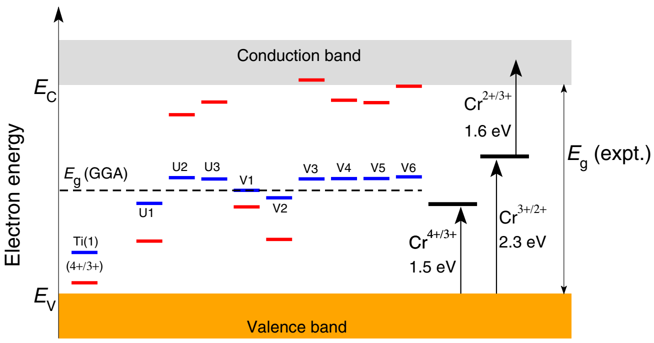

FIG. 10. (Color online) Tentative Cr_{Ti} defect energy levels in h-BaTiO_3 derived from optical absorption spectra [13] (thick black solid lines on the right side) compared with transition levels obtained from the formation energy of defects. Blue lines and red lines are the transition levels obtained from E_{form} (referenced with band gap from GGA shown as dashed line) and $E_{\text{form}}^{\text{PP}}$, respectively. E_{V}, E_{C}, and E_{g} are top of valence band, bottom of conduction band, and the band gap (chosen as 3.5 eV), respectively.

hand, the defect complex configurations where the V_O is in the next-neighbor oxygen shell have shallow transition levels towards the CB.

The shortcomings in the accurate description of the correlation effects and the lack of accountability for the excited states in DFT could be a major factor contributing to some errors. Although we are aware of several reports which account for better description of defect transition levels in ZnO and GaN using hybrid density functional calculations, we remain without any speculation in this regard as the hybrid functional treatment could not be practically applied to such large supercells as used in our calculations.

V. CONCLUSION

By systematically studying numerous configurations and charge states of defects in Cr-doped hexagonal $BaTiO_3$ we have identified the stable defects for different environmental partial pressures of oxygen. The studies were performed with first-principles density functional theory calculations in order to compute the defect formation energies and the charge transition levels. The theoretical results were compared to the experimental findings.

Our results show that the Cr impurities are invariably associated with oxygen vacancies for a wide range of growth conditions where the oxidation state of Cr is found to be 3+ as the most probable. Cr occupies the Ti lattice sites with higher preference for Ti(2) than Ti(1). The oxygen vacancy is more favorable at a position away from the nearest neighbor to the Cr impurity atom. These conclusions are in agreement with the EPR measurements of Cr-doped h-$BaTiO_3$ ceramic samples.

The transition level for the $Cr^{3+} - V_O$ defect complex is found to be sensitive to the configuration of V_O with respect to the Cr atom in the complex configuration. The complexes with V_O and Cr as nearest neighbors give a deep transition level in the band gap, while configurations where the V_O and Cr have larger distances produce shallow transition levels. The optical absorption spectra are used to analyze the defect transition levels in the band gap. The results show some systematics in the relative probability of defects found in the sample for different growth conditions. Yet, a direct comparison of defect transition levels to the peaks in optical spectra could not be achieved leading to open questions which must be tackled in future.

ACKNOWLEDGMENT

The work is funded by the Deutsche Forschungsgemeinschaft through the Collaborative Research Center SFB 762 “Functionality of Oxide Interfaces”.

APPENDIX: POSTPROCESSING OF FORMATION ENERGY

A charged supercell with a compensating jellium background charge allows us to study the charged defects in the supercell approach [50,57–61]. However, due to the finite size of the supercell and together with the limitations of the GGA in predicting the band gap of semiconductors, the formation energies obtained have shortcomings. A set of postprocessing corrections is proposed by Lany and Zunger [48] in order to improve the quality of formation energies derived from the GGA total energies. The different terms of the postprocessing corrections are added to the formation energy obtained from GGA (E_{form}) to give the postprocessed formation energy $E^{\mathrm{PP}}_{\mathrm{form}}$. The $E^{\mathrm{PP}}_{\mathrm{form}}$ is given as

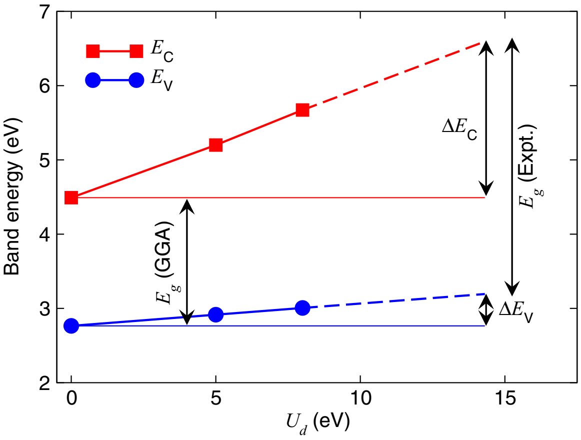

FIG. 11. (Color online) E_V and E_C as a function of U applied on the d orbital of Ti in h-$BaTiO_3$. The extrapolation of the band energies to obtain the experimental band gap of E_g (Expt.) = 3.4 eV gives the value of ΔE_V and ΔE_C, respectively, which are used for the postprocessing of Eq. (A1).

$$
\begin{aligned}
E^{\mathrm{PP}}_{\mathrm{form}} = E_{\mathrm{form}} + q\left(\Delta E_V + (1+f)\left[\frac{q\alpha_M}{2\epsilon L}\right] + \left(V^r_{D,q} - V^r_H\right)\right) \\
- \sum_{n,\vec{k}} \omega_{\vec{k}} \eta_{n,\vec{k}} (e_{n,\vec{k}} - \tilde{e}_C)\Theta(e_{n,\vec{k}} - \tilde{e}_C) \\
+ z_e \Delta E_C - z_h \Delta E_V. \qquad \text{(A1)}
\end{aligned}
$$

Here, ΔE_V and ΔE_C are the relative shifts of the valence band and conduction band edges, respectively. This is estimated by comparing the electronic structure obtained from GGA and GGA+U methods ($U = 5.0$ eV [62] and 8.0 eV on Ti d orbitals) and extrapolating it to get the experimental E_g of pure h-$BaTiO_3$ as shown in Fig. 11. The values of ΔE_V and ΔE_C are obtained as 0.43 eV and 2.10 eV, respectively.

The variables α_M, ϵ, and L are the Madelung constant, relative permittivity, and size of the supercell (estimated from supercell volume), respectively. The values $\alpha_M = 62.95$ [63] and $\epsilon = 57$ [64] are taken from literature. The proportionality factor f for the image charge correction is taken as −0.34, which holds for the fcc lattice [48].

$V^r_{D,q}$ and V^r_H are the average electrostatic potentials over a sphere around an atomic site far from the defect obtained from the defective supercell and the pure host supercell, respectively. The difference of $V^r_{D,q}$ and V^r_H in Eq. (A1) ensures the band alignment which arises due to the chemical shift of supercells with different composition. Due to the presence of inequivalent Ti sites, we have aligned the average V^r_H obtained from Ti(1) sites for the $Cr_{Ti(2)}$ defect and vice versa for $Cr_{Ti(1)}$.

The band-filling effect of the Moss-Burstein type is negligible as the defect concentration in our study is sufficiently low (1.85 mol %). The variables associated with this correction term, namely, $\omega_{\vec{k}}$, $\eta_{n,\vec{k}}$, $e_{n,\vec{k}}$, and $\tilde{e}_C$, are the k-point weight, band occupation, band energies of defect supercell, and the conduction band edge of pure host (after the potential alignment is done as stated above). Θ is the Heaviside step function.

The correction term for the shallow level shifts with respect to the host band edges is calculated by adding (subtracting) the product of the number of electrons z_e (number of holes z_h) and the shift in band level ΔE_C (ΔE_V) discussed in the previous paragraph. The mutually exclusive factors z_e and z_h are obtained by integrating the DOS of the electronic and hole states, respectively.

[1] R. D. Burbank and H. T. Evans, The crystal structure of hexagonal barium titanate, Acta Crystallogr. **1**, 330 (1948).

[2] Kevin W. Kirby and Barry A. Wechsler, Phase relations in the barium titanate–titanium oxide system, J. Am. Ceram. Soc. **74**, 1841 (1991).

[3] R M Glaister and H F Kay, An investigation of the cubic-hexagonal transition in barium titanate, Proc. Phys. Soc. **76**, 763 (1960).

[4] D. Kolar, U. Kunaver, and A. Renik, Exaggerated anisotropic grain growth in hexagonal barium titanate ceramics, Phys. Status Solidi A **166**, 219 (1998).

[5] John G. Dickinson and Ronald Ward, Some new compounds having the hexagonal barium titanate structure, J. Am. Chem. Soc. **81**, 4109 (1959).

[6] E. Sawaguchi, Y. Akishige, T. Yamamoto, and J. Nakahara, Phase transition in hexagonal type $BaTiO_3$, Ferroelectrics **95**, 29 (1989).

[7] J. G. Dickson, Lewis Katz, and Roland Ward, Compounds with the hexagonal barium titanate structure, J. Am. Chem. Soc. **83**, 3026 (1961).

[8] H. T. Langhammer, T. Müller, K-H. Felgner, and H.-P. Abicht, Crystal structure and related properties of manganese-doped barium titanate ceramics, J. Am. Ceram. Soc. **83**, 605 (2000).

[9] G. M. Keith, M. J. Rampling, K. Sarma, N. M. Alford, and D. C. Sinclair, Synthesis and characterisation of doped 6H-$BaTiO_3$ ceramics, J. Eur. Ceram. Soc. **24**, 1721 (2004).

[10] S. Jayanthi and T. R. N. Kutty, Dielectric properties of 3*d* transition metal substituted $BaTiO_3$ ceramics containing the hexagonal phase formation, J. Mater. Sci.: Mater. Electron. **19**, 615 (2008).

[11] Y. Li, Q. Liu, T. Yao, Z. Pan, Z. Sun, Y. Jiang, H. Zhang, Z. Pan, W. Yan, and S. Wei, Hexagonal $BaTi_{1-x}Co_xO_3$ phase stabilized by Co dopants, Appl. Phys. Lett. **96**, 091905 (2010).

[12] R. Böttcher, E. Erdem, H. T. Langhammer, T. Müller, and H.-P. Abicht, Incorporation of chromium into hexagonal barium titanate: An electron paramagnetic resonance study, J. Phys.: Condens. Matter **17**, 2763 (2005).

[13] H. T. Langhammer, T. Müller, R. Böttcher, and H.-P. Abicht, Structural and optical properties of chromium-doped hexagonal barium titanate ceramics, J. Phys.: Condens. Matter **20**, 085206 (2008).

[14] R. Böttcher, H. T. Langhammer, T. Müller, and H.-P. Abicht, 3C–6H phase transition in $BaTiO_3$ induced by Fe ions: An electron paramagnetic resonance study, J. Phys.: Condens. Matter **20**, 505209 (2008).

[15] R. Böttcher, H. T. Langhammer, and T. Müller, Paramagnetic resonance study of nickel ions in hexagonal barium titanate, J. Phys.: Condens. Matter **23**, 115903 (2011).

[16] H. T. Langhammer, T. Müller, R. Böttcher, and H.-P. Abicht, Crystal structure and related properties of copper-doped barium titanate ceramics, Solid State Sci. **5**, 965 (2003).

[17] H. T. Langhammer, T. Müller, K.-H. Felgner, and H.-P. Abicht, Influence of strontium on manganese-doped barium titanate ceramics, Mater. Lett. **42**, 21 (2000).

[18] H.-J. Hagemann and H. Ihrig, Valence change and phase stability of 3*d*-doped $BaTiO_3$ annealed in oxygen and hydrogen, Phys. Rev. B **20**, 3871 (1979).

[19] M. T. Buscaglia, V. Buscaglia, M. Viviani, P. Nanni, and M. Hanuskova, Influence of foreign ions on the crystal structure of $BaTiO_3$, J. Eur. Ceram. Soc. **20**, 1997 (2000).

[20] F. Ren, S. Ishida, and S. Mineta, Effect of manganese addition on phase stability of hexagonal $BaTiO_3$, J. Ceram. Soc. Jpn. **102**, 105 (1994).

[21] A. Feteira, K. Sarma, N. M. Alford, I. M. Reaney, and D. C. Sinclair, Microwave dielectric properties of gallium-doped hexagonal barium titanate ceramics, J. Am. Ceram. Soc. **86**, 511 (2003).

[22] S.-F. Wang, Y.-C. Hsu, J. P. Chu, and C.-H. Wu, Hexagonal $Ba(Ti_{1-x}Mn_x)O_3$ ceramics: Microstructural evolution and microwave dielectric properties, Appl. Phys. Lett. **88**, 042909 (2006).

[23] F. Zhao, Z. Yue, J. Pei, H. Zhuang, Z. Gui, and L. Li, Structure and microwave dielectric properties of hexagonal $Ba[Ti_{1-x}(Ni_{1/2}W_{1/2})_x]O_3$ ceramics, J. Am. Ceram. Soc. **90**, 2461 (2007).

[24] G. V. Lewis and C. R. A. Catlow, Defect studies of doped and undoped barium titanate using computer simulation techniques, J. Phys. Chem. Solids **47**, 89 (1986).

[25] M. T. Buscaglia, V. Buscaglia, M. Viviani, and P. Nanni, Atomistic simulation of dopant incorporation in barium titanate, J. Am. Ceram. Soc. **84**, 376 (2001).

[26] C. L. Freeman, J. A. Dawson, H.-R. Chen, J. H. Harding, L.-B. Ben, and D. C. Sinclair, A new potential model for barium titanate and its implications for rare-earth doping, J. Mater. Chem. **21**, 4861 (2011).

[27] F. M. Michel-Calendini and P. Moretti, Electronic structures of Co(II) and Co(III) impurities in cubic perovskite hosts, Phys. Rev. B **27**, 763 (1983).

[28] P. Moretti and F. M. Michel-Calendini, Impurity energy levels and stability of Cr and Mn ions in cubic $BaTiO_3$, Phys. Rev. B **36**, 3522 (1987).

[29] P. Moretti and F. M. Michel-Calendini, Theoretical active impurity levels of iron, chromium, and manganese for photorefractive effects in barium titanate, J. Opt. Soc. Am. B **5**, 1697 (1988).

[30] M. Actis and F. Michel-Calendini, Impurity levels and nonlinear optical properties of doped $BaTiO_3$ from extended cluster LDA calculations, Int. J. Quantum Chem. **61**, 657 (1997).

[31] J. A. Dawson, C. L. Freeman, L.-B. Ben, J. H. Harding, and D. C. Sinclair, An atomistic study into the defect chemistry of hexagonal barium titanate, J. Appl. Phys. **109**, 084102 (2011).

[32] J. A. Dawson, C. L. Freeman, J. H. Harding, and D. C. Sinclair, Phase stabilisation of hexagonal barium titanate doped with transition metals: A computational study, J. Solid. State. Chem. **200**, 310 (2013).

[33] T. A. Colson, M. J. S. Spencer, and I. Yarovsky, A DFT study of the perovskite and hexagonal phases of $BaTiO_3$, Comput. Mater. Sci. **34**, 157 (2005).

[34] S. K. Nayak, W. A. Adeagbo, H. T. Langhammer, W. Hergert, T. Müller, and R. Böttcher, Study of charged defects for substitutionally doped chromium in hexagonal barium titanate from first-principles theory, Phys. Status Solidi RRL **8**, 527 (2014).

[35] G. Kresse and J. Furthmüller, Efficiency of *ab initio* total energy calculations for metals and semiconductors using a plane-wave basis set, Comput. Mater. Sci. **6**, 15 (1996).

[36] G. Kresse and J. Furthmüller, Efficient iterative schemes for *ab initio* total-energy calculations using a plane-wave basis set, Phys. Rev. B **54**, 11169 (1996).

[37] G. Kresse and D. Joubert, From ultrasoft pseudopotentials to the projector augmented-wave method, Phys. Rev. B **59**, 1758 (1999).

[38] J. P. Perdew, Unified theory of exchange and correlation beyond the local density approximation, in *Electronic Structure of Solids '91*, Physical Research, Vol. 17, edited by P. Ziesche and H. Eschrig (Akademie Verlag, Berlin, 1991), pp. 11–20.

[39] J. Akimoto, Y. Gotoh, and Y. Oosawa, Refinement of hexagonal $BaTiO_3$, Acta Crystallogr. C **50**, 160 (1994).

[40] G. A. Baraff and M. Schlüter, Electronic structure, total energies, and abundances of the elementary point defects in GaAs, Phys. Rev. Lett. **55**, 1327 (1985).

[41] S. B. Zhang and John E. Northrup, Chemical potential dependence of defect formation energies in GaAs: Application to Ga self-diffusion, Phys. Rev. Lett. **67**, 2339 (1991).

[42] Jörg Neugebauer and Chris G. Van de Walle, Atomic geometry and electronic structure of native defects in GaN, Phys. Rev. B **50**, 8067 (1994).

[43] C. Persson, Y.-J. Zhao, S. Lany, and A. Zunger, n-type doping of $CuInSe_2$ and $CuGaSe_2$, Phys. Rev. B **72**, 035211 (2005).

[44] C. G. Van de Walle and J. Neugebauer, First-principles calculations for defects and impurities: Applications to III-nitrides, J. Appl. Phys. **95**, 3851 (2004).

[45] K. Reuter and M. Scheffler, Composition, structure, and stability of RuO_2 (110) as a function of oxygen pressure, Phys. Rev. B **65**, 035406 (2001).

[46] M. W. Chase Jr., *NIST-JANAF Thermochemical Tables*, 4th ed. (American Chemical Society Washington, DC, 1998).

[47] A. J. Cohen, P. Mori-Sánchez, and W. Yang, Insights into current limitations of density functional theory, Science **321**, 792 (2008).

[48] S. Lany and A. Zunger, Assessment of correction methods for the band-gap problem and for finite-size effects in supercell defect calculations: Case studies for ZnO and GaAs, Phys. Rev. B **78**, 235104 (2008).

[49] J. Heyd, G. E. Scuseria, and M. Ernzerhof, Hybrid functionals based on a screened Coulomb potential, J. Chem. Phys. **118**, 8207 (2003).

[50] C. Freysoldt, B. Grabowski, T. Hickel, J. Neugebauer, G. Kresse, A. Janotti, and C. G. Van de Walle, First-principles calculations for point defects in solids, Rev. Mod. Phys. **86**, 253 (2014).

[51] A. Janotti and C. G. Van de Walle, Native point defects in ZnO, Phys. Rev. B **76**, 165202 (2007).

[52] A. Janotti and C. G. Van de Walle, LDA+U and hybrid functional calculations for defects in ZnO, SnO_2, and TiO_2, Phys. Status Solidi B **248**, 799 (2011).

[53] E. Ertekin, V. Srinivasan, J. Ravichandran, P. B. Rossen, W. Siemons, A. Majumdar, R. Ramesh, and J. C. Grossman, Interplay between intrinsic defects, doping, and free carrier concentration in $SrTiO_3$ thin films, Phys. Rev. B **85**, 195460 (2012).

[54] R. Böttcher, H. T. Langhammer, and T. Müller, Jahn-Teller effect in $BaTiO_3 : Cr^{5+}$: An electron paramagnetic resonance study, J. Phys.: Condens. Matter **21**, 075904 (2009).

[55] R. Böttcher, H. T. Langhammer, and T. Müller, The influence of domains on tetrahedrally coordinated Cr^{5+} in ferroelectric $BaTiO_3$: An electron paramagnetic resonance study, J. Phys.: Condens. Matter **21**, 435901 (2009).

[56] S. Eden, S. Kapphan, H. Hesse, V. Trepakov, V. Vikhnin, I. Gregora, Jastrabik. L., and J. Seglins, Observations of the absorption, infrared emission, and excitation spectra of Cr in $BaTiO_3$, J. Phys.: Condens. Matter **10**, 10775 (1998).

[57] P. A. Schultz and A. H. Edwards, Modeling charged defects inside density functional theory band gaps, Nucl. Instrum. Methods Phys. Res., Sect. B **327**, 2 (2014).

[58] E. G. Seebauer and M. C. Kratzer, Charged point defects in semiconductors, Mater. Sci. Eng. R **55**, 57 (2006).

[59] C. W. M. Castleton, A. Höglund, and S. Mirbt, Managing the supercell approximation for charged defects in semiconductors: Finite-size scaling, charge correction factors, the band-gap problem, and the *ab initio* dielectric constant, Phys. Rev. B **73**, 035215 (2006).

[60] J. Lento, J.-L. Mozos, and R. M. Nieminen, Charged point defects in semiconductors and the supercell approximation, J. Phys.: Condens. Matter **14**, 2637 (2002).

[61] G. Makov and M. C. Payne, Periodic boundary conditions in *ab initio* calculations, Phys. Rev. B **51**, 4014 (1995).

[62] D. D. Sante, K. Yamauchi, and S. Picozzi, Beyond standard local density approximation in the study of magnetoelectric effects in $Fe/BaTiO_3$ and $Co/BaTiO_3$ interfaces, J. Phys.: Condens. Matter **25**, 066001 (2013).

[63] A. Sabry, M. Ayadi, and A. Chouikh, Simulation of ionic crystals and calculation of electrostatic potentials, Comput. Mater. Sci. **18**, 345 (2000).

[64] J. A. Dawson, J. H. Harding, H. Chen, and D. C. Sinclair, First-principles study of intrinsic point defects in hexagonal barium titanate, J. Appl. Phys. **111**, 094108 (2012).